Science of the Total Environment 703 (2020) 135563

Contents lists available at ScienceDirect

Science of the Total Environment

journal homepage: www.elsevier.com/locate/scitotenv

Seasonal cycles of lakes on the Tibetan Plateau detected by Sentinel-1 SAR data

Yu Zhang [a], Guoqing Zhang [b,c,*], Tingting Zhu [d]

[a] Chinese Antarctic Center of Surveying and Mapping, Wuhan University, Hubei, China
[b] Key Laboratory of Tibetan Environmental Changes and Land Surface Processes, Institute of Tibetan Plateau Research, Chinese Academy of Sciences, Beijing, China
[c] CAS Center for Excellence in Tibetan Plateau Earth Sciences, Beijing, China
[d] State Key Laboratory of Information Engineering in Surveying, Mapping and Remote Sensing, Wuhan University, Hubei, China

HIGHLIGHTS

- Large lakes (>100 km^2) reached peaks later (August–September) than small lakes (50–100 km^2 in June–July).
- Seasonal cycles for endorheic lakes were more pronounced than exorheic lakes.
- Glacier-fed lakes exhibited delayed peaks relative to non-glacier-fed lakes.
- Large-scale atmospheric circulation systems affect seasonal cycles of TP's lakes.

GRAPHICAL ABSTRACT

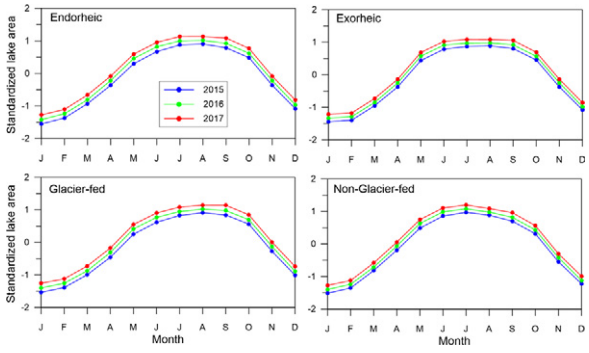

ARTICLE INFO

Article history:
Received 13 July 2019
Received in revised form 28 October 2019
Accepted 15 November 2019
Available online 18 November 2019

Editor: Ouyang Wei

Keywords:
Intra-annual lake mapping
Endorheic lake
Glacier-fed lake
Large-scale atmospheric circulation

ABSTRACT

The long-term evolution of lakes on the Tibetan Plateau (TP) could be observed from Landsat series of satellite data since the 1970s. However, the seasonal cycles of lakes on the TP have received little attention due to high cloud contamination of the commonly-used optical images. In this study, for the first time, the seasonal cycle of lakes on the TP was detected using Sentinel-1 Synthetic Aperture Radar (SAR) data with a high repeat cycle. A total of approximately 6000 Level-1 scenes were obtained that covered all large lakes (>50 km^2) in the study area. The images were extracted from stripmap (SM) and interferometric wide swath (IW) modes that had a pixel spacing of 40 m in the range and azimuth directions. The lake boundaries extracted from Sentinel-1 data using the algorithm developed in this study were in good agreement with in-situ measurements of lake shoreline, lake outlines delineated from the corresponding Landsat images in 2015 and lake levels for Qinghai Lake. Upon analysis, it was found that the seasonal cycles of lakes exhibited drastically different patterns across the TP. For example, large size lakes (>100 km^2) reached their peaks in August–September while lakes with areas of 50–100 km^2 reached their peaks in early June–July. The peaks of seasonal cycles for endorheic lakes were more pronounced than those for exorheic lakes with flat peaks, and glacier-fed lakes with additional supplies of water exhibited delayed peaks in their seasonal cycles relative to those of non-glacier-fed lakes. Large-scale atmospheric circulation systems, such as the westerlies, Indian summer

* Corresponding author at: Key Laboratory of Tibetan Environmental Changes and Land Surface Processes, Institute of Tibetan Plateau Research, Chinese Academy of Sciences, Beijing, China.
E-mail address: guoqing.zhang@itpcas.ac.cn (G. Zhang).

https://doi.org/10.1016/j.scitotenv.2019.135563

monsoon, transition in between, and East Asian summer monsoon, were also found to affect the seasonal cycles of lakes. The results of this study suggest that Sentinel-1 SAR data are a powerful tool that can be used to fill gaps in intra-annual lake observations.

1. Introduction

There are ~1200 lakes with areas larger than 1 km^2 on the Tibetan Plateau (TP), and ~160 lakes larger than 50 km^2 (Zhang et al., 2014b). Lakes on the TP are predominantly distributed in the Inner TP, where there is an endorheic basin linking the various water related features. More than 80% of lakes in the TP have dramatically expanded since ~1995 driven primarily by increased precipitation and the influx of water from melting glaciers (Biskop et al., 2016; Zhang et al., 2017c). The lake area increase is comparable in area to the reductions for waterbodies in other regions of China (Zhang et al., 2019b) and globally on other continents (Pekel et al., 2016) as a consequence of intensive human activities.

The lakes on the TP are important indicators of climate variability in terms of lake area/level/volume changes (Lei et al., 2014; Yang et al., 2017; Zhang et al., 2014b), water surface temperatures (Zhang et al., 2014a), and lake ice phenology (Cai et al., 2019; Kropáček et al., 2013). However, it has been difficult to maintain continuous observations of water temperatures and ice phenology across regions with moderate resolution imaging spectroradiometer (MODIS) data due to its sparse spatial resolution (>250 m) and frequent cloud cover (daily cloud cover of >45%) (Yu et al., 2016). For example, the number of lakes with available surface temperatures (Zhang et al., 2014a) and lake ice data (Cai et al., 2019) is approximately 60, which is much smaller than the approximately 160 lakes >50 km^2 in size (Zhang et al., 2014b). The lake boundaries used in previous studies were primarily extracted from Landsat multi-spectral scanner (MSS) (~79 m) and thematic mapper (TM)/enhanced thematic mapper plus (ETM+)/operational land imager (OLI) (30 m) data, all of which exhibited good performance in tracking the associated changes (Zhang et al., 2017b) for even small glacial lakes in the Himalayas (Li and Sheng, 2012). These applications typically employ Landsat data collected around October of each year as lake boundary is relatively stable at that time of year (Zhang et al., 2017a) and the available data in other seasons is often obscured by high cloud cover (Yu et al., 2016). Therefore, many previous studies have focused on the long-term trend of lake evolution since the beginning of the satellite era (e.g. Pekel et al., 2016; Zhang et al., 2017b). This results in a sparse interval of intra-annual lake area (one sample each year), which is not sufficient to capture the seasonal cycle of lakes. The knowledge of variabilities of lake surface water extent in the TP are scarce as the lack of dense observations from satellite images. Although the seasonal variability of lakes can also be observed by lake level from in-situ measurements (Lei et al., 2017), only a small amount of lakes is available. On the TP, the lake level trends are consistent with those of lake area or volume changes as flat shorelines that undergo natural evolution (i.e., without human intervention) (Zhang et al., 2017c). This suggests that capturing lake areas with more comprehensive observations of seasonal cycles can be used as an effective indicator of lake changes in response to climate change.

In the TP, the biggest limitation for lake area mapping using mid and high spatial resolution optical satellite images, such as Landsat and Sentinel-2, is cloud contamination. In contrast, synthetic aperture radar (SAR) sensors are capable of capturing images in all weather conditions. Many studies have shown the potential of satellite SAR data for mapping lakes. For example, TerraSAR-X and Radarsat-2 data have been employed for mapping small lakes in the southwest of France (Baup et al., 2014) and glacial lake detection in the Alps, Pamir, and Himalayas (Strozzi et al., 2012). In addition, ENVISAT Advanced Synthetic Aperture Radar (ASAR) images have been used to detect variations in lake inundation areas (Medina et al., 2008; Medina et al., 2010). However, the temporal resolution of these data is longer than 35 days. In contrast, Sentinel-1 SAR imagery has higher repeat cycle dates that can be used to obtain intra-month lake area observations and Sentinel-1 images have been successfully used for monitoring lake inundation areas (Zeng et al., 2017), mapping glacial lakes (Miles et al., 2017; Wangchuk et al., 2019), monitoring flood situations (Cazals et al., 2016; Twele et al., 2016; Westerhoff et al., 2013), analyzing ice motion (Nagler et al., 2015), and conducting earthquake analyses (Sun et al., 2016).

This study is the first to monitor the seasonal cycles of large lakes across the entire TP by investigating the changes in intra-month lake areas using Sentinel-1 data for 165 large lakes (>50 km^2) (Fig. 1). The differences of lake seasonal cycles for endorheic lakes against exorheic lakes, glacier-fed lakes against non-glacier-fed lakes, and relationship with large-scale atmosphere circulation patterns are analyzed. The observation of lake areas via SAR imagery will benefit in understanding the processes of lake changes, intra-annual lake changes in response to climatic change, and lake water balance simulation across the TP.

2. Materials and methods

2.1. Study area

The TP in central Asia has a mean elevation of 4000 m above sea level (a.s.l.) and an area of 3×10^6 km^2 (above 2500 m a.s.l.) (Zhang et al., 2013). The TP is known as the water tower of Asia and supplies fresh water via the Asia's major rivers to about 2 billion people downstream. The surface hydrological landscape of the TP is characterized by an extensive and dense distribution of lakes, snowpack, glaciers, and permafrost. The lakes on the TP account for approximately 50% of number and area in China (Ma et al., 2010; Zhang et al., 2019b). The alpine lakes are an important indicator and sentinel of climatic change.

The average monthly minimum and maximum air temperature from China Meteorological Administration (CMA) weather stations on the TP is about −10 °C in winter and ~10 °C in summer, respectively (Fig. S1). Most of the precipitation (60–90%) falls in June–September and gradually decreases from the southeast to the northwest (Fig. S2) (Kang et al., 2010). The TP is overall getting warmer and wetter during the past decades, which is comparable with trend of lake area changes (Kuang and Jiao, 2016; Zhang et al., 2017b). Climate on the TP is mainly influenced by the westerlies in winter and the Asian monsoon in summer (Maussion et al., 2014). The overall pattern of glacier mass balance in the TP and surroundings is accelerating loss, but it is spatial heterogeneous, i.e. great negative magnitude in the southeast, and almost stable state in the northwest (Brun et al., 2017; Yao et al., 2012). The high mountains are mainly located on the periphery of the TP, the interior TP is relative flat with most of large lakes there.

The lakes in this study were grouped based on sizes, types of water-feed, and the impact of large-scale atmosphere circulation systems as part of analyzing the seasonal cycle of lakes. The lakes are divided into four types based on their sizes: >1000, 500–1000, 100–500, and 50–100 km^2. Five lakes had an area larger than 1000 km^2 and included Qinghai Lake, Selin Co, Nam Co, Chibzhang Co/Dorsoidong Co, and Zhari Namco. The lakes are also classified as endorheic (closed or hydrologically landlocked) or exorheic (outflow) lakes based on geomorphological feature, glacier-fed or non-glacier-fed lakes by water-feed types (Tables S1–2). In addition, the lakes are separated into four groups

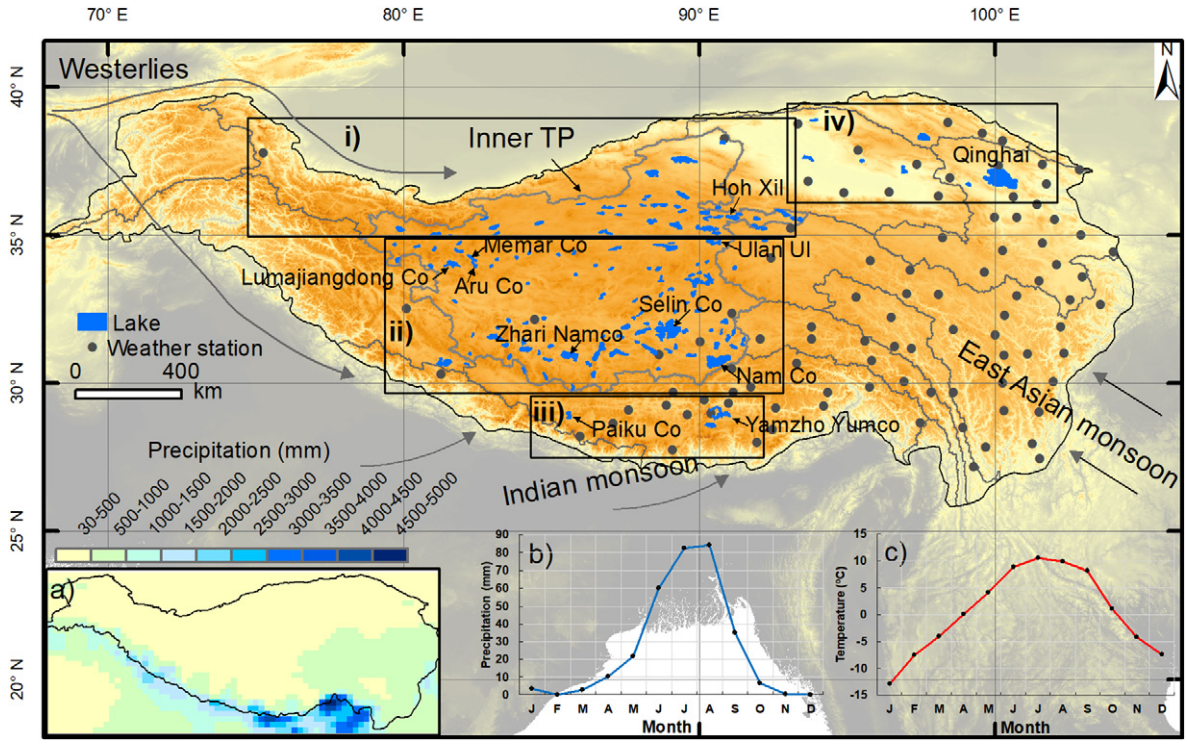

Fig. 1. Distribution of lakes in the TP based on available Sentinel-1 data. The insets show: a) the mean annual precipitation from the Global Precipitation Climatology Centre (GPCC) between 2010 and 2013, b) the monthly precipitation from meteorological stations in the Inner TP between 2015 and 2016, and c) the monthly temperatures obtained from meteorological stations in the Inner TP between 2015 and 2016. Locations of China Meteorological Administration (CMA) meteorological stations are denoted. Zones i, ii, iii and iv are Northwestern TP, Central TP, Southern TP and Northeastern TP, respectively.

including the westerlies, Indian summer monsoon, transition in between, and East Asian summer monsoon based on large-scale atmosphere circulation systems.

2.2. Data sources

2.2.1. Sentinel-1 data

As a part of the Global Monitoring for Environment and Security (GMES) program, the Sentinel-1A satellite was launched on 3 April 2014 and now operates in a near-polar, sun-synchronous orbit with a 12-day repeat time. After the launch of Sentinel-1B in 2016, the Sentinel-1 constellation system is able to provide spatial resolution up to 40 m and high temporal resolution up to a 6-day observation. Sentinel-1A and B are equipped with a C-band SAR payload (~5.4 GHz). Sentinel-1 supports four different operative modes: stripmap (SM), wave (WV), interferometric wide swath (IW), and extra wide swath (EW) (Amitrano et al., 2014). The spatial resolution of Sentinel-1 is comparable to that of Landsat TM/ETM+/OLI (30 m) and superior to the 250 or 500 m MODIS (Miles et al., 2017). The 12-day temporal resolution for both Sentinel-1A and Sentinel-1B are comparable to the 16-day Landsat-8, especially in terms of its cloud penetration capabilities. Sentinel-1 and other missions (e.g., Sentinel-2–6) demonstrate the high potential for cryospheric observations (Malenovský et al., 2012; Miles et al., 2017).

In this study, approximately 6000 Level-1 ground range detected (GRD) scenes between 2015 and 2017 were downloaded from the European Space Agency (ESA) Scientific Data Hub (https://scihub.copernicus.eu/). Lake boundary extraction in this study via the SM and IW modes, which provide single polarization in HH (H for horizontal polarization) or VV (V for vertical polarization) channels and dual polarization in HH + HV or VH + VV channels. Both modes provide a pixel spacing of 40 m in the range and azimuth directions with swath widths of 80 and 250 km, respectively. The incidence angles of these two modes range from 18.3°– 46.8° and 29.1°– 47.0°.

A total of 5940 Sentinel-1 scenes was sufficient to cover all of lake regions of interest (Fig. 2) and the imaging dates of the available Sentinel-1 data in the TP were normally distributed between the 10th to the 20th of each month with the maximum number falling on the 15th day.

The total lake area delineated respectively from the available data for the 1st–10th days, 11th–20th days, and 21st–31st days, and the average area delineated in each month were compared to identify the most representative data (Fig. 2). In general, the trends in the seasonal cycle were similar between these ranges, although a slight increase was observed in the total lake area from the 1st–10th days to the 21st–31st days between January and September and a decrease was observed from October to December. The total lake area in 11th–20th days was similar to the mean total area from these dates. When the date histogram of the available data and total lake area in the various data composites were evaluated, the lake areas from the 11th–20th days of each month were selected.

2.2.2. Data used for validation

In-situ lake shoreline measurements for Aru Co, an inland lake located in the northwestern TP (Fig. 1), were conducted in July 2017 by a high-precision GPS. Aru Co was known widely for two glacier collapses in western Tibet in July 2016 (Tian et al., 2017). The collapsed ice rushed down and reached into Aru Co. The collected lake shoreline trace data were used to validate lake boundary extracted from Sentinel-1 data.

The performance of Sentinel-1 data in mapping lake area was also indirectly verified by comparison with lake area delineated from Landsat TM/OLI images. Moreover, lake area extracted from Sentinel-1 was also compared with lake levels from in-situ measurements for

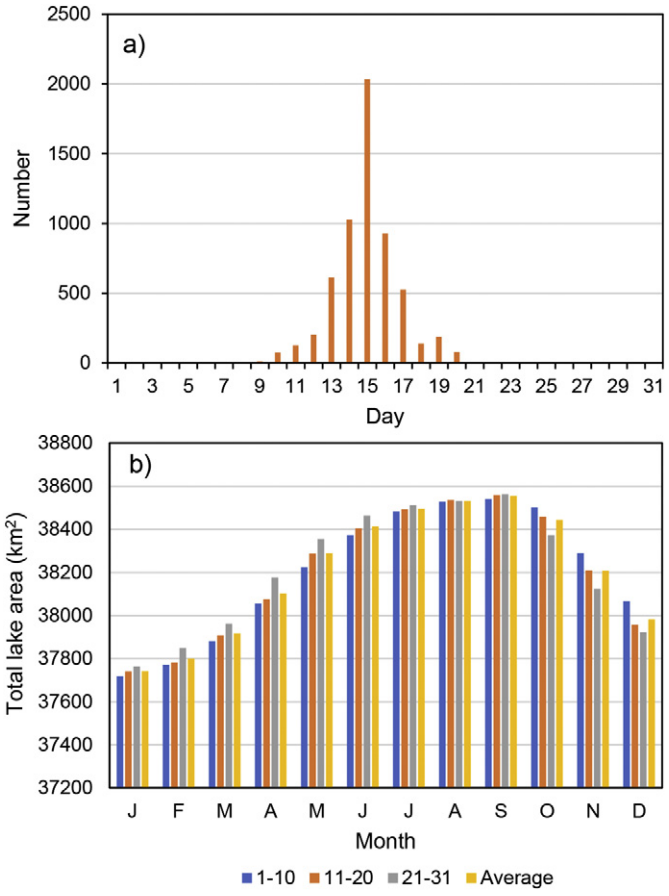

Fig. 2. Histogram of the lake areas from Sentinel-1A observations in the TP between 2015 and 2017. a) Number of available images in each month. b) Total lake area in each month in terms of the data available from the 1st–10th days, 11th–20th days, 21st–31st days, and the average for one month.

Qinghai Lake as the daily lake levels for this lake are available and correspond well to lake area in previous study (Zhang et al., 2011a).

2.3. Methods

The process of extracting lake boundaries from Sentinel-1 data consists of two steps: data preprocessing and lake mapping. A detailed flowchart of this process is shown in Fig. 3.

2.3.1. Preprocessing

The topographical characteristics of interest include the aspect, slope, roughness, all of which can cause significant brightness areas in the near-range and dark areas in the far-range as the local area is not projected into the plane perpendicular to slant range (Small, 2011). Moreover, heterogeneity in the range or azimuth directions may further impact the intensity and amplitude of SAR backscattering signals. In addition, the SM and IW modes have a large angle of incidence range, which may lead to significant variation in the backscatter coefficient from the near-range to the far-range. Thus, a radiometric correction factor must be applied to accurately represent the relationship between backscattering coefficient and reference angle. In this study, a cosine law based radiometric correction was used (Gauthier et al., 1998; Mladenova et al., 2013). By assuming the backscattering power was re-radiated in the upper hemisphere, the measured backscatter can be described as Eqs. (1) and (2):

$$\sigma^0_{\theta_i} = \sigma^0_0 \, cos^2(\theta_i) \tag{1}$$

$$\sigma^0_{ref} = \frac{\sigma^0_{\theta_i} \, cos^n(\theta_{ref})}{cos^n(\theta_i)} \tag{2}$$

where σ^0_0 is the backscatter independent of incident angle, the measured backscatter ${\sigma_{\theta_i}}^0$ is related to ground surface roughness n, which can be derived from the slope of the measured backscatter ${\sigma_{\theta_i}}^0$ and the local incident angle θ_i using linear regression, and i means the i-th pixel in the SAR image. The reference angle θ_{ref} is the central incidence angle of the SAR scene. The corrected SAR backscatter can be calculated by subtracting the backscatter values of SAR and noise pattern. Finally, a radiation calibration method was utilized to convert digital numbers (DN) in SAR image to backscatter σ^0 in dB as Eq. (3).

$$\sigma^0_i = \left(\mathrm{DN}_i^2 - noise_{ifull}\right) / \left(\sigma^0_{i\,full}\right)^2 \tag{3}$$

where $noise_{ifull}$ is the noise floor and it is a function of range, $\sigma^0_{i\,full}$ is sigmaNough. For Sentinel-1 data, the input is usually given in unit 16 format. Both noise floor and SigmaNough are obtained from LUT (Look-up Table).

The monthly radiometric corrections for both lake and background land-cover were illustrated in Fig. 4. For each month, 1000 pixels of lake (Qinghai Lake as a sample) and background were used to calculate the backscattering during radiometric correction. Before correction in Fig. 4(a), the backscattering during lake frozen period from December to next March overlaps together. From May to October, lake has the

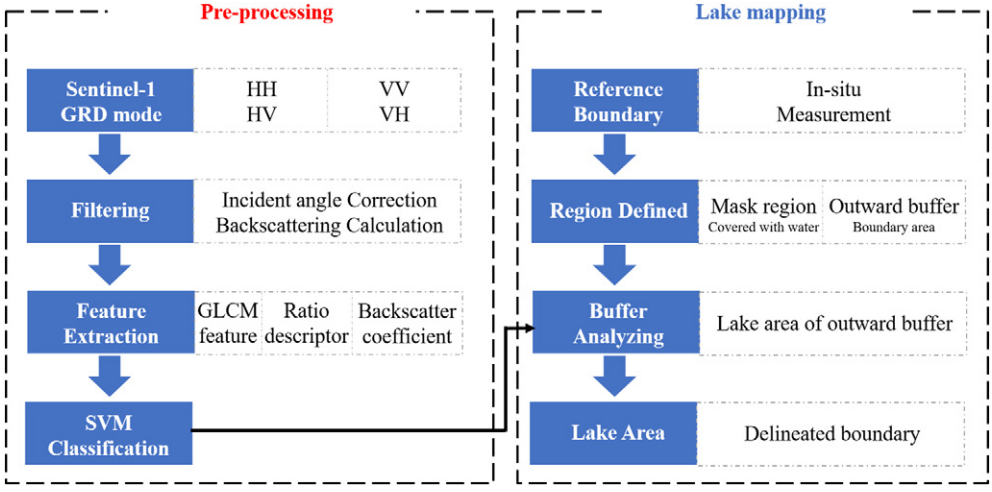

Fig. 3. Flowchart of the process of extracting lake areas from Sentinel-1 data. GLCM: gray level co-occurrence matrix; HH, HV, VV, VH represent different polarization, where the first letter means transmit polarization and the second one means receive polarization.

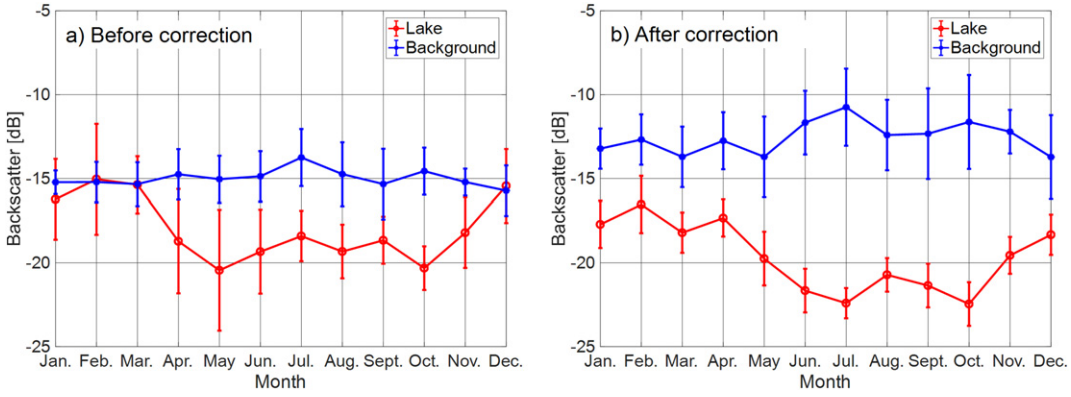

Fig. 4. Backscatter of lake water and background land-cover before and after radiometric correction of Sentinel-1 image with Qinghai Lake as a sample.

larger backscatter value compared with background. After radiometric correction in Fig. 4(b), there is a significant decrease of backscatter in lake and increase in background, which results in a better contrast of image feature between them. Moreover, the variance of lake backscattering also decreased after correction, which indicates that the feature descriptor for lake will become more stable after correction.

The next step is to extract the features, including SAR backscatter and gray level co-occurrence matrix (GLCM) (Lumb and Sethi, 2013) texture calculation. The GLCM features are a type of textural descriptor that computes the similarity of different pixels over a given distance using statistical methods. In this study, the GLCM features include the mean value, standard deviation, energy, contrast, homogeneity, correlation, and entropy, all of which can be computed as Eqs. (4)–(9):

$$S_d(i,j) = \frac{P_d(i,j)}{\sum_{i=1}^{K=1}\sum_{j=1}^{K} P_d(i,j)} \tag{4}$$

$$\text{Energy} = \sum_{i=1}^{k=1}\sum_{j=1}^{K}[S_d(i,j)]^2 \tag{5}$$

$$\text{Homogeneity} = \sum_{i=1}^{k=1}\sum_{j=1}^{K}\frac{S_d(i,j)}{1+(i+j)^2} \tag{6}$$

$$\text{Contrast} = \sum_{i=1}^{k=1}\sum_{j=1}^{K}(i-j)^2 S_d(i,j) \tag{7}$$

$$\text{Correlation} = \frac{\sum_{i=1}^{k=1}\sum_{j=1}^{K}(i-\mu_x)\left(j-\mu_y\right)S_d(i,j)}{\sigma_x\sigma_y} \tag{8}$$

$$\text{Entropy} = \sum_{i=1}^{k=1}\sum_{j=1}^{K} S_d(i,j)\ log_{10}S_d(i,j) \tag{9}$$

where S_d is GLCM. Each cell (i,j) is the relative frequency measurements of two pixels occurrence with gray level i and j, respectively, and it is separated by co-occurrence distance d. $P_d(i,j)$ is the second-order statistical probability between two gray level i and j. μ_x, μ_y is mean value in rows and columns, and σ_x, σ_y is the corresponding standard deviation of different cells. The GLCM features consist of GLCM in Eq. (4) and the corresponding texture feature based on GLCM. For the GLCM features, the window size is 16×16 in both height and width directions, the separated distance d is 8, the number of steps is 16, and the gray level K is 32. In addition, for dual-polarization data, the ratio of two different polarization channels in dB is also used as a feature descriptor in the classification steps.

2.3.2. Lake mapping

Lake boundaries mapped from Landsat OLI images in 2015–2017 were used to compare the performance from Sentinel-1 data with Qinghai Lake as a sample. The water and other land covers are distinguished using normalized difference water index (NDWI) (Mcfeeters, 1996) with optimal threshold selected based on the Otsu method (Otsu, 1979). In addition, the lake boundaries mapped from Landsat data (Zhang et al., 2017b) were used as a reference and an inward buffer of 3 km was used as a mask region for each lake that was defined as a constant area that is always covered by water. Excluding this constant water area can significantly reduce the computation time required to identify water. An outward buffer of 3 km was also applied based on the reference boundary as a target region to distinguish water from land. It was assumed that any changes in lake shoreline due to expansion or shrinkage occurred within the buffered regions ($\pm$3 km along the reference outline). A properly delineated lake area is a combination of the constant water region and lake water within the outward buffer region.

The task of separating water and non-water features in the outward buffer region was accomplished using the support vector machine (SVM) classification algorithm (Cortes and Vapnik, 1995). By mapping the input feature vectors, including the backscattering, GLCM feature, and polarization ratio, into a high dimensional feature space, the radial basis function (RBF) kernel based on the SVM was adapted to identify lake water and background pixels (Hsu et al., 2003). Here, the default parameters in the SVM classifier were used with a kernel factor $\gamma = 0.1$ and a margin parameter $C = 1$.

Besides, a set of feature descriptors were selected by analyzing the variations in normalized value corresponding to the defined lake water and background with several combinations of obtained parameters. Using GLCM energy feature as an example, quantization gray level $K = 32$, window size 16×16, moving step 16 indicate the best result since the normalized value between water body and background has the largest interval (Fig. 5a, b). For the optimal value of separated distance, $d = 8$ shows a relatively better results with the normalized interval of larger than 0.1, while some features perform similar normalized value with $d = 4$. Moreover, in Fig. 5c and d, the optimal parameter selection in SVM classifier, some features such as energy, contrast and entropy in HH channel and energy, correlation, homogeneity and entropy in HV channel show clear differences between lake and background land-cover. The above parameters were found to provide a tradeoff between noise reduction, detail preservation and correct classification.

The Sentinel-1 imagery was preprocessed using Python toolbox and the extraction of the regions was performed by ArcGIS software package. The SVM classification algorithms, including the feature extraction and classification, were executed on the MATLAB 2016b platform.

The uncertainty in mapping lake areas is usually estimated based on the length of lake shoreline and pixel size (Fujita et al., 2009; Salerno et al., 2012). In this study, the error in the delineated lake area was assumed to be $\pm 0.5 \times$ lake perimeter $\times$ 40 m (pixel size) (Salerno et al., 2012).

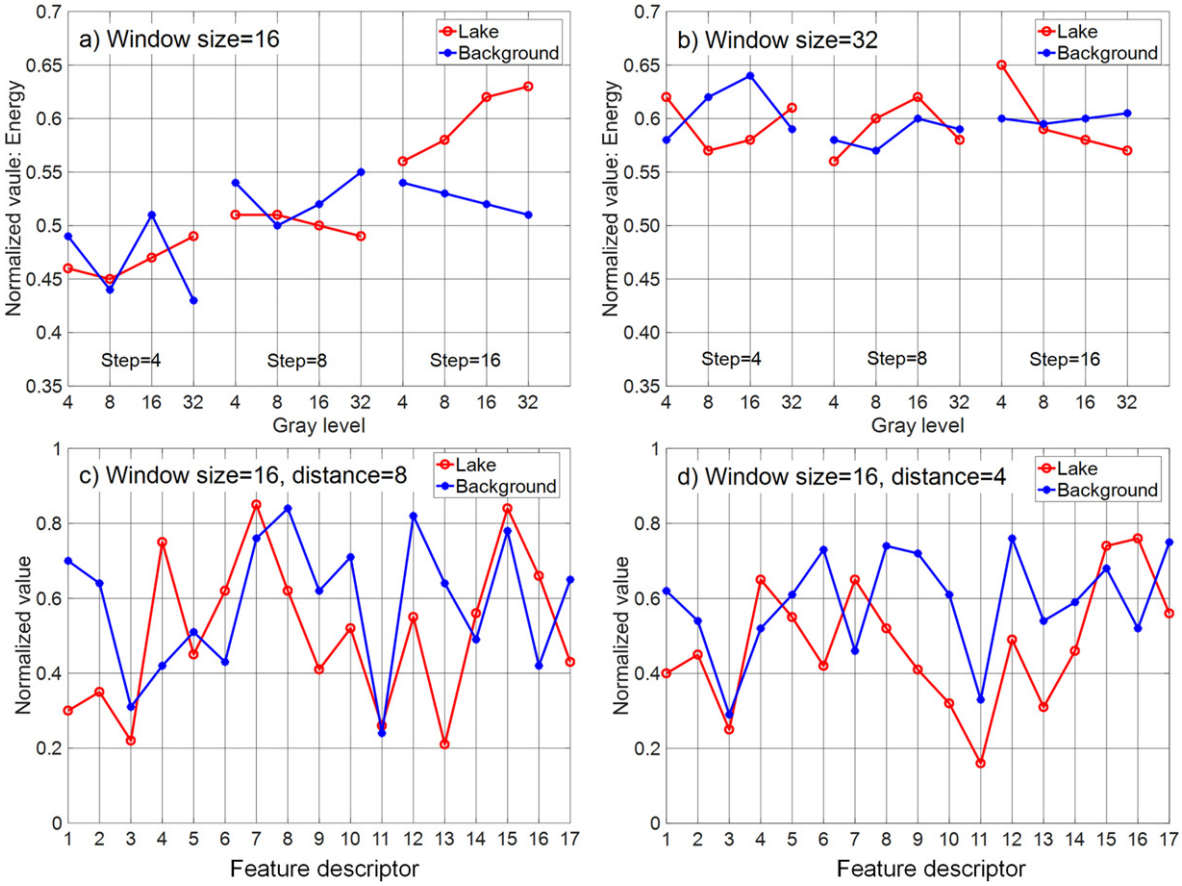

Fig. 5. Parameter selection for SVM classifier with Qinghai Lake as a sample. (For *x* label in c and d, 1 = Backscatter, 2 = mean, 3 = variance, 4 = Energy, 5 = Homogeneity, 6 = Contrast, 7 = Correlation, 8 = Entropy for HH or VV channel, 9–16 are the same feature descriptor for HV or VH channel, 17 = Ratio).

3. Results and discussion

3.1. Performance of Sentinel-1 in delineating lake area

The monthly area for 165 large lakes (>50 km^2) from 2015 to 2017 were mapped (Table S3). The errors of lake area delineated from Sentinel-1 data compared with lake shoreline measurements of Aru Co in the northwestern TP ranged from 10 to 55 m, with the mean value of 21.4 m, which is less than a pixel of Sentinel-1 (40 m) (Fig. 6a).

The lake area for these large lakes observed using Landsat and Sentinel-1 in 2015 shows a high correlation (r^2 = 0.99) (Fig. 6b), which suggests that the lake area obtained from Sentinel-1 is suitable for lake boundary mapping. Moreover, this data was adopted in several previous studies for examining the extent of water and good results were achieved (Huang et al., 2018; Tian et al., 2017; Wangchuk et al., 2019; Zeng et al., 2017).

In addition, the lake area obtained from Sentinel-1 data was compared with lake level time series obtained from in-situ measurements of Qinghai Lake on the corresponding dates. Overall, the lake area matched well with water level, although some anomalies were noted in early 2015 and late in 2017, which could be due to water freezing (Fig. 6c). The correlation between lake area from Sentinel-1 and the measured lake levels was high (r^2 = 0.89) (Fig. 6d). Comparisons of in-situ measurements of lake shoreline with lake boundary from Sentinel-1, lake area between Sentinel-1 and Landsat data, and lake area and water level support the use of Sentinel-1 data for highly efficient lake area observations.

Several large lakes in different climatic regions were selected to illustrate the method of data processing and the accuracy of water classification (Fig. 7). For ten large lakes selected, the areas for six were overestimated by 0.06% to 0.35%, while the other four were underestimated by −0.11% to −0.56%. For example, Qinghai Lake, which is the largest saltwater lake in China, had an area of 4375.92 ± 18.11 km^2 on 13 September 2015 as observed from Landsat data, while the area derived from Sentinel-1 data on 15 September 2015 was 4378.37 ± 18.14 km^2. The inconsistency in the water classification was primarily caused by an island in the southeast region that was detected by Landsat but not the Sentinel-1. This discrepancy was probably due to the 30-m spatial resolution Landsat versus the 40-m spatial resolution of Sentinel-1. Selin Co (the largest lake in Tibet) had an area of 2402.58 ± 15.67 km^2 on 5 July 2015 from Landsat data, but its area on 12 July 2015 based on Sentinel-1 data was 2405.74 ± 15.69 km^2 with an overestimated by 0.13%. Despite these differences, the overall mismatch in lake boundary observations was small.

At present, only Qinghai Lake on the TP has continuous in-situ measurements of lake level referenced to a geodetic reference system (i.e., the Yellow Sea Datum). This limits us to use water level from Qinghai Lake as one validation site only. Sentinel-1 SAR data is also used to map small glacial lakes in the Himalaya (Wangchuk et al., 2019) and to extract river surface (Sghaier et al., 2017). The potential of Sentinel-1 SAR data with high temporal resolution (6-day) and spatial resolution (~20 m) could be further explored. Besides the associated climate changes in this study, Sentinel-1 SAR data has also significant advantage over widely used optical satellite data in monitoring cryosphere hazards such as mapping potential dangerous glacial lakes on the TP.

3.2. Lake seasonal cycle across the TP

The total lake area across all seasons increased each year from 2015 to 2017 and the lake seasonal cycle shows for lakes larger than 100 km^2

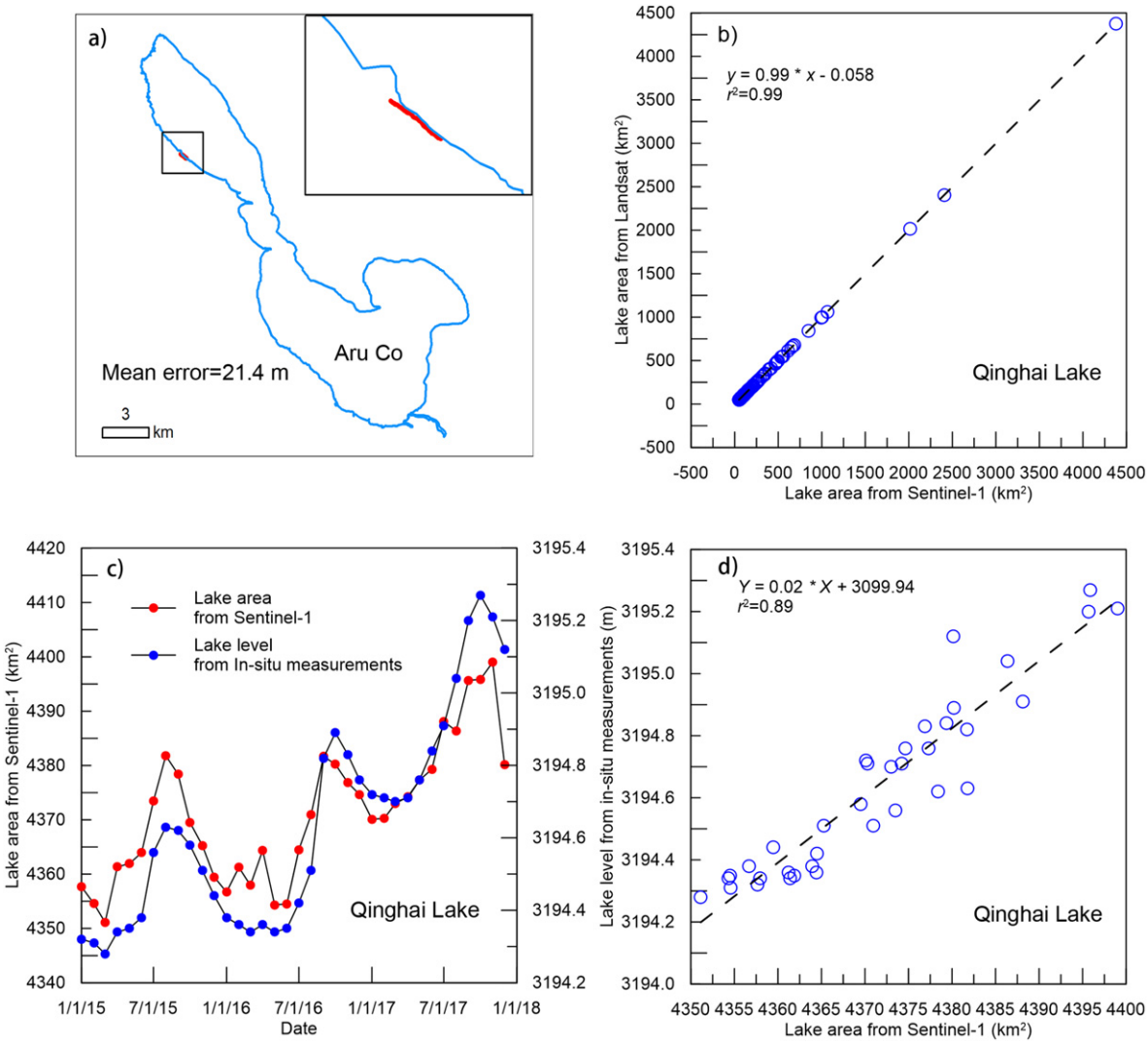

Fig. 6. Comparisons of lake mapping from Sentinel-1 and in-situ measurements and Landsat data. a) Comparison of shorelines from Sentinel-1 data and in-situ measurements for Aru Co in 2017. b) Lake area from Sentinel-1 and Landsat for Qinghai Lake in 2015. c) Time series of lake area from Sentinel-1 and lake level from in-situ measurements for Qinghai Lake in 2015–2017. d) Correlation between lake area from Sentinel-1 and lake level from in-situ measurements for Qinghai Lake in 2015–2017.

in size, the lake area expanded from January to August/September and contracted after September (Fig. 8). However, lakes with areas in the range of 50–100 km^2 reached their maximum area in June/July and contracted thereafter. This implies that smaller lakes reach their peaks earlier compared with larger lakes.

The differences between lakes of different sizes may be because larger lakes (>100 km^2) have larger lake basins (or a larger area ratio of lake basin to lake) relative to smaller lakes (50–100 km^2). In addition, lakes on the TP are usually fully covered by ice in mid-January and are ice free in early July (Cai et al., 2019) and the extent of lake water can expand during the frozen period. In addition, the Asia monsoon can bring rainfall in June–August (Fig. 1), which can supply water to lakes and cause the lakes to expand. Finally, delays in the precipitation-induced runoff in lake basin can postpone lake expansion until about September, and this is especially true for large lakes.

Overall, the lakes on the TP show the continuous area expansion during 2015–2017, which is consistent with annual lake observations from Landsat images (Zhang et al., 2019a). The seasonal difference of maximum lake area could be correlated with lake basin size. For example, lake area changes are positively related with supply coefficient (Lei et al., 2014; Song et al., 2014). Especially for lakes on the TP, the expansion is dominantly driven by increased precipitation (Zhang et al., 2017c). A larger lake basin (>100 km^2 each lake) can supply more water discharge to lake, which delays the peaks of maximum lake area relative to small lake basin (50–100 km^2 each lake). In present study, only large lakes (>50 km^2) are examined. This study provides a direction that the comprehensive, high temporal-spatial resolution, and continuous lake mapping become possible.

Seasonal cycles for endorheic lakes were found to be more pronounced than those for exorheic lakes, which have flat peaks during the summer season (Fig. 9). This may be attributed to differences between the closed nature of endorheic lakes versus both water inflows and outflows of exorheic lakes. The closed lake basin can reflect regional water cycle faster than outflowing lake basin, which is directly indicated by difference of seasonal lake extent in this study. The difference of lake level changes between endorheic and exorheic lakes are also apparent. The closed lakes have higher rates of lake level rising compared with outflowing lakes (Zhang et al., 2017c). In particular, some outflowing lakes show lake level decrease, although the terminal closed lakes have lake level increase (Song et al., 2013; Zhang et al., 2011b). Therefore, the seasonal cycle can indicate the difference of water cycle processes between endorheic and exorheic lakes.

Distinct differences were observed in lake seasonal cycle between glacier-fed and non-glacier-fed lakes. The peaks for glacier-fed lakes appeared in July–September, but the peaks for non-glacier-fed lakes appeared earlier in June–July. The melting of glaciers provided an

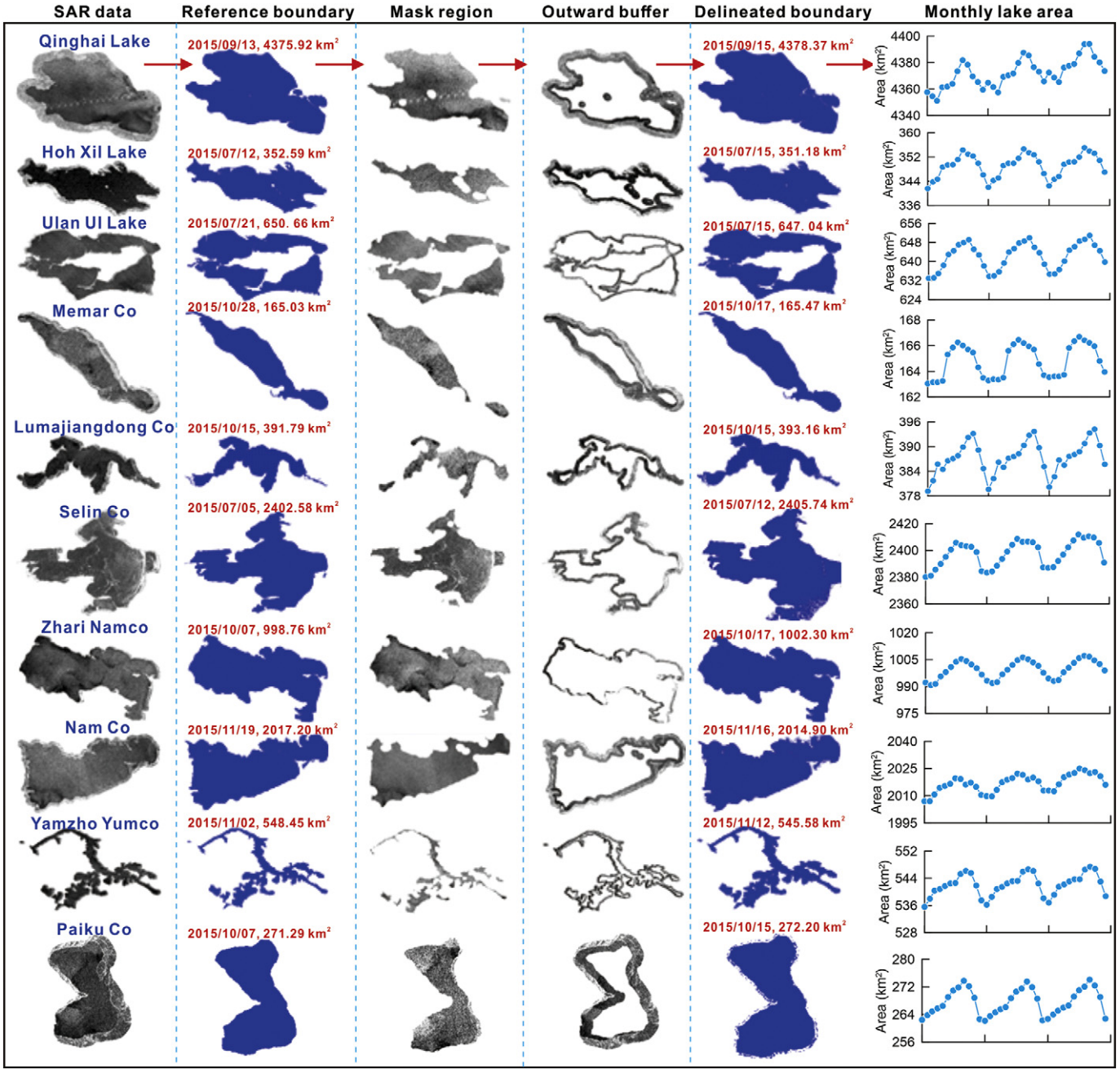

Fig. 7. Examples showing the process of data processing for typical lakes in different climatic regions. The original Sentinel-1 SAR data, reference lake boundaries obtained from Landsat imagery, static lake masks derived from the inside buffering, buffers covering the region over which the lake boundary changes, lake boundaries extracted from Sentinel-1 data, and a time series of the monthly lake area are shown by column. The locations and names of these ten lakes are labeled in Fig. 1.

additional water supply for lake basins with glacier coverage that was not available to those supplied by rainfall alone. The glacier-melt water delayed lake expansion until September. Similarly, this can be observed from lake level changes. The glacier-fed lakes exhibit faster lake level increase against no-glacier-fed lakes as glacier meltwater supply augmented lake surface precipitation and precipitation runoff (Song et al., 2014). The glacier meltwater can still supply lakes only if the temperature is above 0 °C even the monsoon-induced precipitation ends earlier.

3.3. Relationship between lake seasonal cycles and large-scale atmosphere circulation patterns

There are several large-scale atmospheric circulation patterns that affect lake seasonal cycles. Moisture is supplied to the TP via the Indian monsoon, mid-latitude westerlies, and south-eastern Asian monsoon (Bothe et al., 2009), and all of these large-scale atmospheric circulation anomalies affect water vapor convergence. Three different domains, namely, the westerlies (northern TP), Indian monsoon (southern TP), and the transition region between about 32°N and 35°N, have been identified via precipitation $\delta^{18}O$ and atmospheric model simulations (Yao et al., 2013). In the TP and surrounding areas, the weakened Indian monsoon and enhanced westerlies have driven the different status of glacier changes (Yao et al., 2012). The lakes in the northwestern TP (region i in Fig. 1) are predominantly driven by the westerlies, in the central TP (region ii) by both the Indian monsoon and westerlies, in the southern TP (region iii) by the Indian summer monsoon, and in the northeastern TP (region iv) by the East Asian summer monsoon (EASM) (An et al., 2012; Xu et al., 2007).

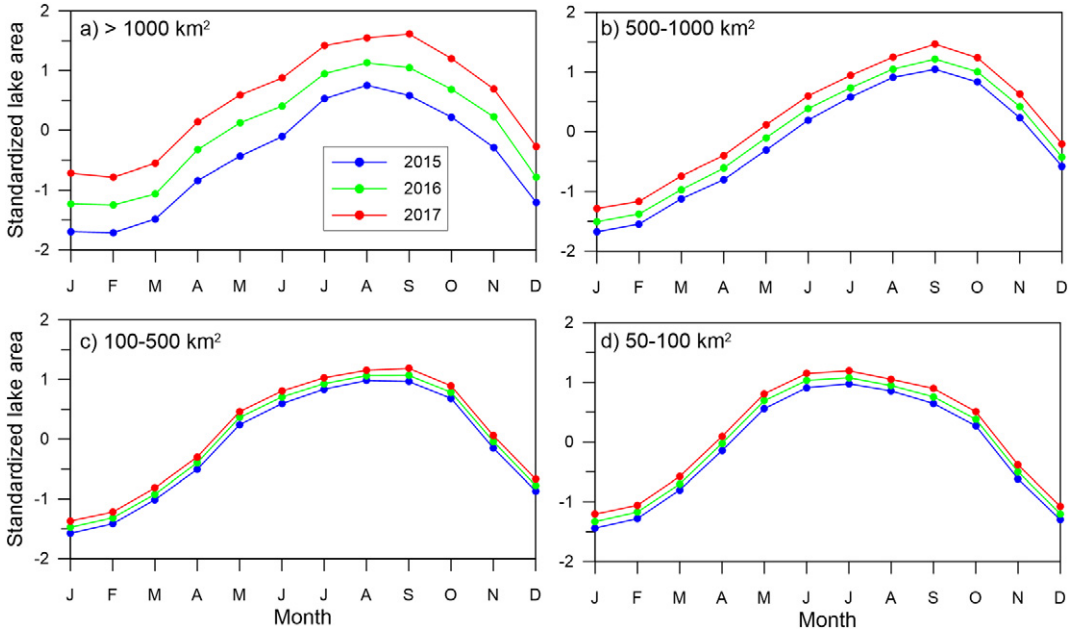

Fig. 8. Standardized monthly lake area cycles for lakes of different sizes from 2015 to 2017. a) Lakes larger than 1000 km^2 in size. b) Lakes 500–1000 km^2 in size. c) Lakes 100–500 km^2 in size. d) Lakes 50–100 km^2 in size.

Lake seasonal cycles in the northwestern TP (the westerlies domain) tend to increase from January to September and decrease after peaking in July–September (Fig. 10). The seasonal cycles in the central TP (transition domain) are similar to those in the northwestern TP. However, lake seasonal cycles in the southern TP (Indian monsoon domain) exhibit a very different pattern and tend to increase continuously from January to September and then decrease after peaking in September. The lakes in the northeastern TP where the EASM is dominant have seasonal cycles similar to those in the northwestern and central TP, although their peaks are in June–August. The differences in lake seasonal cycles in these four zones are primarily driven by the dominant large-scale atmosphere circulation systems. The number and sizes of lakes in the four climatic regions vary. For example, the southern TP includes only three lakes. Differences in the numbers of lakes may result in uncertainties in determining lake seasonal pattern.

The intra-annual lake extents in three climatic domains present different seasonal features. The monthly precipitation displays similar pattern with lake seasonal cycle but they are not matched well in annual scale (Fig. S2), which could be ascribed to limited distribution of CMA weather stations on the TP (Fig. 1). Only five CMA stations are located in the Inner TP, with the dominant lake distribution. For the northwestern TP with many large lakes, only a CMA station far from lakes is available. The sparse and uneven distributions of CMA stations, especially in high altitude regions, are the limitations of

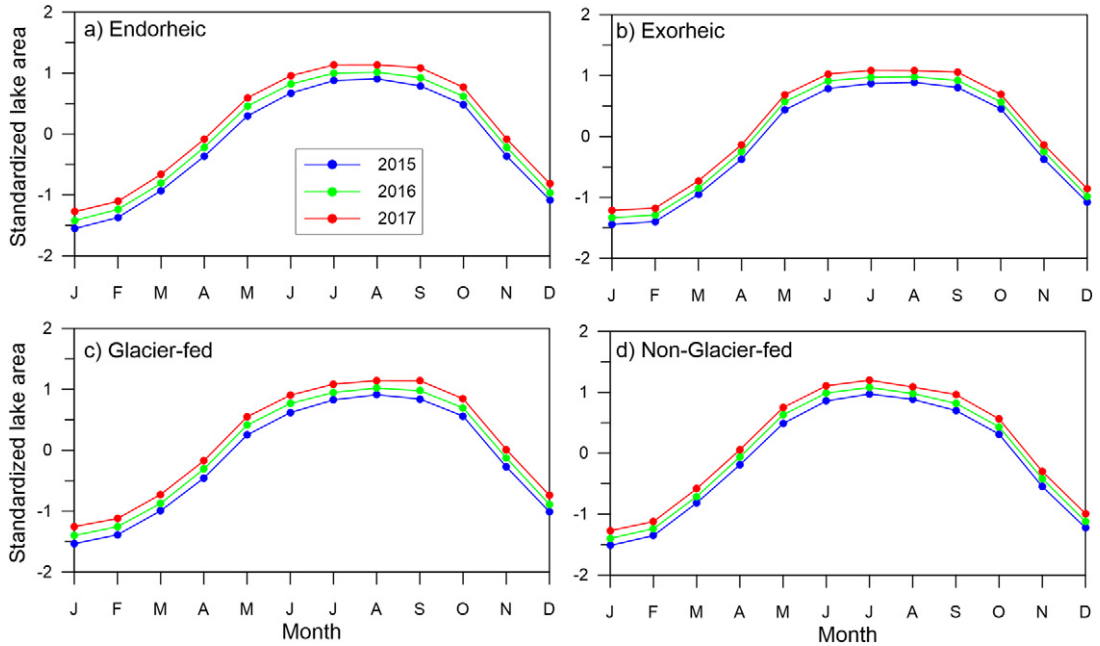

Fig. 9. Standardized monthly lake area cycles from 2015 to 2017. a) Endorheic lakes. b) Exorheic lakes. c) Glacier-fed lakes. d) Non-glacier-fed lakes.

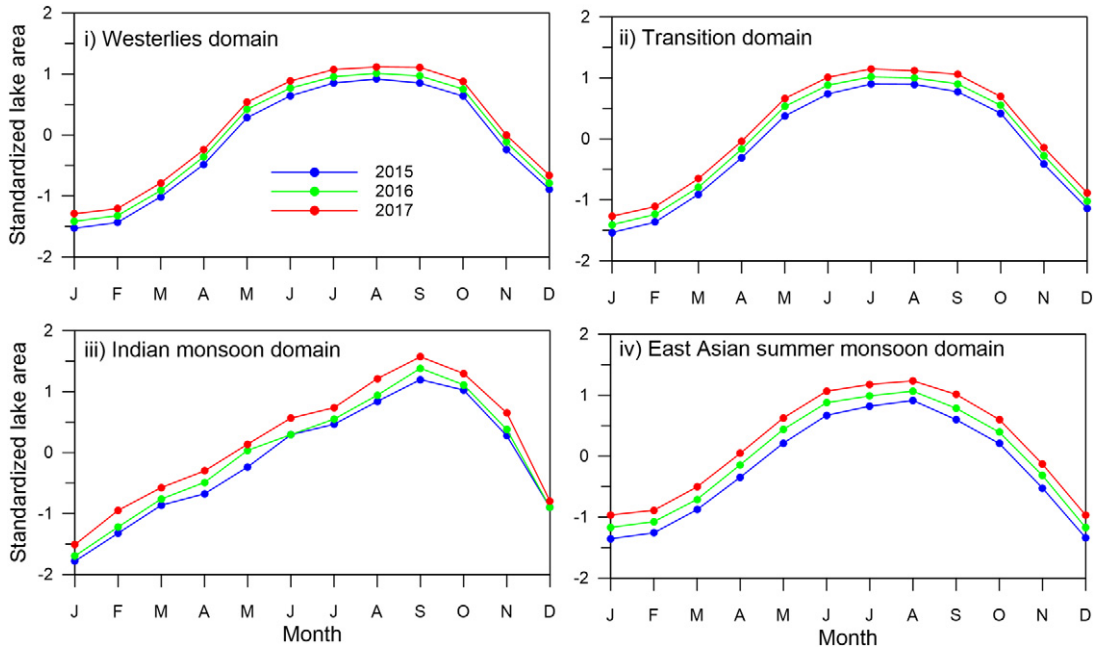

Fig. 10. Standardized seasonal cycles of lake areas in different climatic zones of the TP that are driven by large-scale atmospheric circulation systems. i) Northwestern TP (Westerlies domain). ii) Central TP (Transition domain). iii) Southern TP (Indian monsoon domain). iv) Northeastern TP (East Asian summer monsoon domain). The zone divisions were previously shown in Fig. 1.

detailed examination of lake seasonal cycle with station-based precipitation data. In addition, the difference of lake seasonal cycle in different climatic zones can be illustrated from in-situ lake level observations (Lei et al., 2017). In this study, a comprehensive lake seasonal cycle for 165 large lakes (>50 km^2 each lake) are provided, which can outline seasonal features from large-scale climatic influence better than limited lake level measurements.

4. Conclusions

The inter- and intra-annual variability in lake areas on the TP are an important climatic indicator. The optical satellite images have been successfully used to examine long-term trend of lake area changes. However, lake seasonal cycles have been problematic as optical image is often obscured by cloud cover. SAR data can map lakes with high temporal resolution despite broad cloud cover on the vast TP. In this study, for the first time, the seasonal cycles of 165 large lakes on the TP with each area of >50 km^2 are detected using Sentinel-1 SAR data with a high repeat cycle of 12 days (or 6 days with two satellites) and medium spatial resolution of 40 m. The drastically different patterns in the types and sizes of lakes and the atmospheric circulation systems affecting those lakes across the TP are revealed by analysis of the seasonal cycles of lakes on the TP.

The areas of larger lakes (>100 km^2) were found to peak in August–September while the areas of relatively smaller lakes (50–100 km^2) peaked in early June–July. The endorheic lakes were found to exhibit more pronounced seasonal cycles than exorheic lakes. The glacier-fed lakes present delayed peaks relative to non-glacier-fed lakes due to augmented water supply. In addition, the large-scale atmospheric circulation systems such as the westerlies, Indian monsoon, transition in between, and East Asian summer monsoon were found to control the patterns of lake seasonal cycle. The results of this study demonstrate the high potential of using Sentinel-1 SAR data for detecting seasonal cycles of lakes on the TP. The long-term seasonal cycle of lakes will benefit in understanding the limnological, hydrological, and climate information in the TP.

Declaration of competing interest

The authors declare that they have no known competing financial interests or personal relationships that could have appeared to influence the work reported in this paper.

Acknowledgements

This study was supported by the Natural Science Foundation of China (Grants 41801266, 41871056, 41571068, 41901275), the National Key Research and Development Program of China (2018YFB0505005), and Field station alliance project of Chinese Academy of Sciences (KFJ-SW-YW038). We thank two anonymous reviewers for their constructive comments which has improved this manuscript.

Appendix A. Supplementary data

Supplementary data to this article can be found online at https://doi.org/10.1016/j.scitotenv.2019.135563.

References

Amitrano, D., Martino, G., Iodice, A., Mitidieri, F., Papa, M., Riccio, D., et al., 2014. Sentinel-1 for monitoring reservoirs: a performance analysis. Remote Sens. 6, 10676.
An, Z., Colman, S.M., Zhou, W., Li, X., Brown, E.T., Jull, A.J.T., et al., 2012. Interplay between the Westerlies and Asian monsoon recorded in Lake Qinghai sediments since 32 ka. Sci. Rep. 2.
Baup, F., Frappart, F., Maubant, J., 2014. Combining high-resolution satellite images and altimetry to estimate the volume of small lakes. Hydrol. Earth Syst. Sci. 18, 2007–2020.
Biskop, S., Maussion, F., Krause, P., Fink, M., 2016. Differences in the water-balance components of four lakes in the southern-central Tibetan Plateau. Hydrol. Earth Syst. Sci. 20, 209–225.
Bothe, O., Fraedrich, K., Zhu, X., 2009. The large-scale circulations and summer drought and wetness on the Tibetan Plateau. Int. J. Climatol. 30, 844–855.
Brun, F., Berthier, E., Wagnon, P., Kääb, A., Treichler, D., 2017. A spatially resolved estimate of High Mountain Asia glacier mass balances from 2000 to 2016. Nat. Geosci. 10, 668–673.
Cai, Y., Ke, C., Li, X., Zhang, G., Duan, Z., Lee, H., 2019. Variations of lake ice phenology on the Tibetan Plateau from 2001 to 2017 based on MODIS data. J. Geophys. Res. Atmos. 124, 825–843.

Cazals, C., Rapinel, S., Frison, P.-L., Bonis, A., Mercier, G., Mallet, C., et al., 2016. Mapping and characterization of hydrological dynamics in a coastal marsh using high temporal resolution sentinel-1A images. Remote Sens. 8, 570.
Cortes, C., Vapnik, V., 1995. Support-vector networks. Mach. Learn. 20, 273–297.
Fujita, K., Sakai, A., Nuimura, T., Yamaguchi, S., Sharma, R.R., 2009. Recent changes in Imja Glacial Lake and its damming moraine in the Nepal Himalaya revealed by in situ surveys and multi-temporal ASTER imagery. Environ. Res. Lett. 4, 045205.
Gauthier, Y., Bernier, M., Fortin, J.-P., 1998. Aspect and incidence angle sensitivity in ERS-1 SAR data. Int. J. Remote Sens. 19, 2001–2006.
Hsu, C.-W., Chang, C.-C., Lin, C.-J., 2003. A Practical Guide to Support Vector Classification.
Huang, W., DeVries, B., Huang, C., Lang, M., Jones, J., Creed, I., et al., 2018. Automated extraction of surface water extent from Sentinel-1 data. Remote Sens. 10, 797.
Kang, S.C., Xu, Y.W., You, Q.L., Flugel, W.A., Pepin, N., Yao, T.D., 2010. Review of climate and cryospheric change in the Tibetan Plateau. Environ. Res. Lett. 5, 015101.
Kropáček, J., Maussion, F., Chen, F., Hoerz, S., Hochschild, V., 2013. Analysis of ice phenology of lakes on the Tibetan Plateau from MODIS data. Cryosphere 7, 287–301.
Kuang, X., Jiao, J.J., 2016. Review on climate change on the Tibetan Plateau during the last half century. J. Geophys. Res.: Atmosp. 121, 3979–4007.
Lei, Y., Yang, K., Wang, B., Sheng, Y., Bird, B.W., Zhang, G., et al., 2014. Response of inland lake dynamics over the Tibetan Plateau to climate change. Clim. Chang. 125, 281–290.
Lei, Y., Yao, T., Yang, K., Sheng, Y., Kleinherenbrink, M., Yi, S., et al., 2017. Lake seasonality across the Tibetan Plateau and their varying relationship with regional mass changes and local hydrology. Geophys. Res. Lett. 44, 892–900.
Li, J., Sheng, Y., 2012. An automated scheme for glacial lake dynamics mapping using Landsat imagery and digital elevation models: a case study in the Himalayas. Int. J. Remote Sens. 33, 5194–5213.
Lumb, M., Sethi, P., 2013. Texture feature extraction of RGB, HSV, YIQ and dithered images using GLCM, wavelet decomposition techniques. Int. J. Comput. Appl. 68, 25–31.
Ma, R., Duan, H., Hu, C., Feng, X., Li, A., Ju, W., et al., 2010. A half-century of changes in China's lakes: global warming or human influence? Geophys. Res. Lett. 37, L24106.
Malenovský, Z., Rott, H., Cihlar, J., Schaepman, M.E., García-Santos, G., Fernandes, R., et al., 2012. Sentinels for science: potential of Sentinel-1, -2, and -3 missions for scientific observations of ocean, cryosphere, and land. Remote Sens. Environ. 120, 91–101.
Maussion, F., Scherer, D., Mölg, T., Collier, E., Curio, J., Finkelnburg, R., 2014. Precipitation seasonality and variability over the Tibetan Plateau as resolved by the High Asia Reanalysis. J. Clim. 27, 1910–1927.
McFeeters, S.K., 1996. The use of the normalized difference water index (NDWI) in the delineation of open water features. Int. J. Remote Sens. 17, 1425–1432.
Medina, C.E., Gomez-Enri, J., Alonso, J.J., Villares, P., 2008. Water level fluctuations derived from ENVISAT Radar Altimeter (RA-2) and in-situ measurements in a subtropical waterbody: Lake Izabal (Guatemala). Remote Sens. Environ. 112, 3604–3617.
Medina, C.E., Gomez-Enri, J., Alonso, J.J., Villares, P., 2010. Water volume variations in Lake Izabal (Guatemala) from in situ measurements and ENVISAT Radar Altimeter (RA-2) and Advanced Synthetic Aperture Radar (ASAR) data products. J. Hydrol. 382, 34–48.
Miles, K.E., Willis, I.C., Benedek, C.L., Williamson, A.G., Tedesco, M., 2017. Toward monitoring surface and subsurface lakes on the Greenland Ice Sheet using Sentinel-1 SAR and Landsat-8 OLI imagery. Front. Earth Sci. 5, 58.
Mladenova, I.E., Jackson, T.J., Bindlish, R., Hensley, S., 2013. Incidence angle normalization of radar backscatter data. IEEE Trans. Geosci. Remote Sens. 51, 1791–1804.
Nagler, T., Rott, H., Hetzenecker, M., Wuite, J., Potin, P., 2015. The Sentinel-1 mission: new opportunities for ice sheet observations. Remote Sens. 7, 9371–9389.
Pekel, J.-F., Cottam, A., Gorelick, N., Belward, A.S., 2016. High-resolution mapping of global surface water and its long-term changes. Nature 540, 418–422.
Otsu, N., 1979. A threshold selection method from gray-level histograms. IEEE Trans. Syst. Man Cybern. Syst. 9, 62–66.
Salerno, F., Thakuri, S., D'Agata, C., Smiraglia, C., Manfredi, E.C., Viviano, G., et al., 2012. Glacial lake distribution in the Mount Everest region: uncertainty of measurement and conditions of formation. Glob. Planet Change. 92–93, 30–39.
Sghaier, M.O., Foucher, S., Lepage, R., 2017. River extraction from high-resolution SAR images combining a structural feature set and mathematical morphology. IEEE J. Sel. Top. Appl. Earth Obs. Remote Sens. 10, 1025–1038.
Small, D., 2011. Flattening gamma: radiometric terrain correction for SAR Imagery. IEEE Trans. Geosci. Remote Sens. 49, 3081–3093.
Song, C., Huang, B., Ke, L., 2013. Modeling and analysis of lake water storage changes on the Tibetan Plateau using multi-mission satellite data. Remote Sens. Environ. 135, 25–35.
Song, C., Huang, B., Richards, K., Ke, L., Hien, V.P., 2014. Accelerated lake expansion on the Tibetan Plateau in the 2000s: induced by glacial melting or other processes? Water Resour. Res. 50, 3170–3186.
Strozzi, T., Wiesmann, A., Kääb, A., Joshi, S., Mool, P., 2012. Glacial lake mapping with very high resolution satellite SAR data. Nat. Hazards Earth Sys. Sci. 12, 2487–2498.
Sun, J., Shen, Z.-K., Li, T., Chen, J., 2016. Thrust faulting and 3D ground deformation of the 3 July 2015 Mw 6.4 Pishan, China earthquake from Sentinel-1A radar interferometry. Tectonophysics 683, 77–85.
Tian, H., Li, W., Wu, M., Huang, N., Li, G., Li, X., et al., 2017. Dynamic monitoring of the largest freshwater lake in China using a new water index derived from high spatiotemporal resolution Sentinel-1A data. Remote Sens. 9, 521.
Twele, A., Cao, W., Plank, S., Martinis, S., 2016. Sentinel-1-based flood mapping: a fully automated processing chain. Int. J. Remote Sens. 37, 2990–3004.
Wangchuk, S., Bolch, T., Zawadzki, J., 2019. Towards automated mapping and monitoring of potentially dangerous glacial lakes in Bhutan Himalaya using Sentinel-1 Synthetic Aperture Radar data. Int. J. Remote Sens. 40, 4642–4667.
Westerhoff, R.S., Kleuskens, M.P.H., Winsemius, H.C., Huizinga, H.J., Brakenridge, G.R., Bishop, C., 2013. Automated global water mapping based on wide-swath orbital synthetic-aperture radar. Hydrol. Earth Syst. Sci. 17, 651–663.
Xu, H., Hou, Z.H., Ai, L., Tan, L.C., 2007. Precipitation at Lake Qinghai, NE Qinghai-Tibet Plateau, and its relation to Asian summer monsoons on decadal/interdecadal scales during the past 500 years. Palaeogeogr. Palaeoclimatol. Palaeoecol. 254, 541–549.
Yang, R., Zhu, L., Wang, J., Ju, J., Ma, Q., Turner, F., et al., 2017. Spatiotemporal variations in volume of closed lakes on the Tibetan Plateau and their climatic responses from 1976 to 2013. Clim. Chang. 140, 621–633.
Yao, T., Thompson, L., Yang, W., Yu, W., Gao, Y., Guo, X., et al., 2012. Different glacier status with atmospheric circulations in Tibetan Plateau and surroundings. Nat. Clim. Chang. 2, 663–667.
Yao, T., Masson-Delmotte, V., Gao, J., Yu, W., Yang, X., Risi, C., et al., 2013. A review of climatic controls on $\delta^{18}O$ in precipitation over the Tibetan Plateau: observations and simulations. Rev. Geophys. 51, 525–548.
Yu, J., Zhang, G., Yao, T., Xie, H., Zhang, H., Ke, C., et al., 2016. Developing daily cloud-free snow composite products from MODIS Terra-Aqua and IMS for the Tibetan Plateau. IEEE Trans. Geosci. Remote Sens. 54, 2171–2180.
Zeng, L., Schmitt, M., Li, L., Zhu, X.X., 2017. Analysing changes of the Poyang Lake water area using Sentinel-1 synthetic aperture radar imagery. Int. J. Remote Sens. 38, 7041–7069.
Zhang, G., Xie, H., Duan, S., Tian, M., Yi, D., 2011a. Water level variation of Lake Qinghai from satellite and in situ measurements under climate change. J. Appli. Remote Sens. 5, 053532.
Zhang, G., Xie, H., Kang, S., Yi, D., Ackley, S., 2011b. Monitoring lake level changes on the Tibetan Plateau using ICESat altimetry data (2003−2009). Remote Sens. Environ. 115, 1733–1742.
Zhang, G., Yao, T., Xie, H., Kang, S., Lei, Y., 2013. Increased mass over the Tibetan Plateau: from lakes or glaciers? Geophys. Res. Lett. 40, 2125–2130.
Zhang, G., Yao, T., Xie, H., Qin, J., Ye, Q., Dai, Y., et al., 2014a. Estimating surface temperature changes of lakes in the Tibetan Plateau using MODIS LST data. J. Geophys. Res. Atmos. 119, 8552–8567.
Zhang, G., Yao, T., Xie, H., Zhang, K., Zhu, F., 2014b. Lakes' state and abundance across the Tibetan Plateau. Chin. Sci. Bull. 59, 3010–3021.
Zhang, G., Li, J., Zheng, G., 2017a. Lake-area mapping in the Tibetan Plateau: an evaluation of data and methods. Int. J. Remote Sens. 38, 742–772.
Zhang, G., Yao, T., Piao, S., Bolch, T., Xie, H., Chen, D., et al., 2017b. Extensive and drastically different alpine lake changes on Asia's high plateaus during the past four decades. Geophys. Res. Lett. 44, 252–260.
Zhang, G., Yao, T., Shum, C.K., Yi, S., Yang, K., Xie, H., et al., 2017c. Lake volume and groundwater storage variations in Tibetan Plateau's endorheic basin. Geophys. Res. Lett. 44, 5550–5560.
Zhang, G., Luo, W., Chen, W., Zheng, G., 2019a. A robust but variable lake expansion on the Tibetan Plateau. Sci. Bull. 64, 1306–1309.
Zhang, G., Yao, T., Chen, W., Zheng, G., Shum, C.K., Yang, K., et al., 2019b. Regional differences of lake evolution across China during 1960s–2015 and its natural and anthropogenic causes. Remote Sens. Environ. 221, 386–404.